Nanoscale

Accepted Manuscript

This is an *Accepted Manuscript*, which has been through the Royal Society of Chemistry peer review process and has been accepted for publication.

Accepted Manuscripts are published online shortly after acceptance, before technical editing, formatting and proof reading. Using this free service, authors can make their results available to the community, in citable form, before we publish the edited article. We will replace this *Accepted Manuscript* with the edited and formatted *Advance Article* as soon as it is available.

You can find more information about *Accepted Manuscripts* in the **Information for Authors**.

Journal Name

ARTICLE

Straightforward Synthesis of Bimetallic Co/Pt Nanoparticles in Ionic Liquid: Atomic Rearrangement Driven by Reduction-Sulfidation Processes and Fischer-Tropsch Catalysis

Dagoberto O. Silva,[a] Leandro Luza,[a] Aitor Gual,[a] Daniel L. Baptista,[b] Fabiano Bernardi,[b] Maximiliano J. M. Zapata,[b] Jonder Morais[b] and Jairton Dupont [a]*

Unsupported bimetallic Co/Pt nanoparticles (NPs) of 4.4±1.9 nm can be easily obtained by the simple reaction of [bis(cylopentadienyl)cobalt(II)] and [tris(dibenzilydeneacetone) bisplatinum(0)] complexes in 1-n-butyl-3-methylimidazolium hexafluorophosphate IL at 150°C under hydrogen (10 bar) for 24h. These bimetallic NPs display core-shell like structures in which mainly Pt composes the external shell and its concentration decreases in the inner-shells ($CoPt_3$@Pt-like structure). XPS and EXAFS analysis shows the restructuration of the metal composition at the NP surface when they are submitted to hydrogen and posterior H_2S sulfidation, thus inducing the migration of Co atoms to the external shells of the bimetallic NPs. Furthermore; the isolated bimetallic NPs are active catalysts for the Fischer-Tropsch synthesis, with selectivity for naphtha products.

Introduction

The possibility of tailoring the electronic and geometric structures of bimetallic nanoparticles (NPs) by the addition of a second metal is one of the most important approaches to obtaining more efficient catalysts.[1, 2] In this respect, the catalytic properties are strongly dependent on the structure, composition, and oxidation state of the surface of bimetallic catalysts.[3-6] Among the most studied bimetallic metal nanoparticles (MNPs), those composed of Co/Pt are some of the most investigated with regard to their applications in fuel cell devices, nanosensors and catalysis.[4, 7-11] The presence of a second metal can increase the catalytic properties (oxidation or reduction, for instance) of the other metal.[12] For example the presence of Co in bimetallic Co/Pt NPs exhibited a remarkable improvement in CO tolerance and electrochemical activity as compared to monometallic Pt NPs for direct methanol fuel cells.[8] Conversely, the presence of Pt can facilitate the reduction of inactive Co oxide formed during catalysis such as in Fischer-Tropsch synthesis (FTS). Indeed, the formation of metal oxides is almost unavoidable due to reactivity of the reduced Fe or Co towards oxidation under the FT reaction

conditions. The use of catalysts, usually bimetallic, to facilitate the reduction of metal oxide to active species under the FT reaction conditions is one of the solutions that has been investigated.[13] In general, the promotion of supported cobalt catalysts with noble metals such as Ru, Pt or Pd modifies both the catalyst structure and catalytic performance (usually with significant beneficial effects in its catalytic performance) in FTS.[14] In particular, the FT reaction can be operated at 433 K in the case of Co/Pt alloys, which is a lower operational temperature than that which is commonly used for conventional catalysts. It is assumed that the formation of Co over-layer structures on Co/Pt alloy NPs is responsible for the unusual catalytic performance. It was proposed that the changes to the transition states imposed by the lattice mismatch between two metals can be used as the basis for the rational design of more active low temperature FTS bimetallic catalysts.[15]

Although there have been various reports on the preparation and use of different types of bimetallic Co/Pt NPs, at least two main aspects have still not been completely resolved. The alloying and de-alloying process of the Co/Pt bimetallic NPs under catalytic conditions has rarely been investigated.[16] Moreover, the morphological transformations, and structural

and compositional variations of bimetallic Co/Pt NPs in the course of the dealloying process were investigated using supported MNPs. Indeed, previous studies have mainly focused on supported disordered Co/Pt alloy catalysts, probably due to particle sintering during the high-temperature annealing that is generally necessary to obtain ordered phases.[17]

Although there are several methods available for the preparation of various types of Co/Pt NPs (alloys, core-shell, etc.), the majority employs supports and/or stabilizing agents such as surfactants/ligands.[4, 17-23] Therefore, the controlled synthesis of unsupported surface "clean" bimetallic Co/Pt metal catalysts still remains a challenge. In this respect, ionic liquids (ILs) have proven to be an adequate media for the chemical (bottom-up) and physical (top-down) generation of surface "clean" metal NPs.[24, 25] In particular, ILs can be used for the preparation of stable and surface "clean" bimetallic NPs.[26-32]

We report that unsupported bimetallic Co/Pt NPs can be easily prepared using the organometallic approach[33] in ionic liquids.[34] The presence of Pt in the bimetallic NPs of 4.4±1.9 nm facilitates the reduction of oxides species at relative very low temperatures (126°C). STEM, HR-TEM, EDS, XRD, XPS and EXAFS analysis showed that these NPs display core-shell like structures ($CoPt_3@Pt$) in which mainly Pt composes the external shell and its concentration decreases in the inner-shells. Moreover, these NPs have been shown to be an interesting model to investigate the metal composition changes when submitted to hydrogen reduction and posterior H_2S sulfidation, which induces the migration of Co atoms to the

external shells of the bimetallic NP. Finally, these unsupported bimetallic NPs are active catalysts for the FTS.

Results and discussion

The organometallic precursors [bis(cylopentadienyl) cobalt(II)] $(Co(Cp)_2)$ and [tris(dibenzilydeneacetone) bisplatinum(0)] $(Pt_2(dba)_3)$ have been chosen as MNP precursors because they possess only hydrocarbon-containing ligands that, by reduction/decomposition, generate organic by-products with poor coordinating properties to the surface of MNPs and can be easily removed from the reaction mixture.[33]

The reaction of a mixture of equimolar amounts of the organometallic Co(II) and Pt(0) complexes in 1-n-butyl-3-methylimidazolium hexafluorophosphate IL at 150°C under 10 bar of molecular hydrogen generates bimetallic Co/Pt NPs of 4.4±1.9 nm, as determined by STEM (Figure 1) and XRD (Figure 2) analysis. It is interesting to note that whatever the proportion of Co/Pt used (1:1 or 1:3), the preferential formation of $CoPt_3@Pt$-like structures was observed, indicating that the IL is somehow driven towards the formation of this type of alloys with Pt-rich NP surface. The formation of this type of core shell like structures could be ascribed to the ability of Pt(0) precursor and/or the Pt(0) species with low nuclearity in the IL, formed by decomposition of the Pt(0) precursor, to catalyze the reduction of Co(II) to Co(0); once part of the Co is consumed, the Pt NPs start to grow due to the low relative rate of Co(II) reduction compared to the decomposition of the Pt(0) precursor.[30]
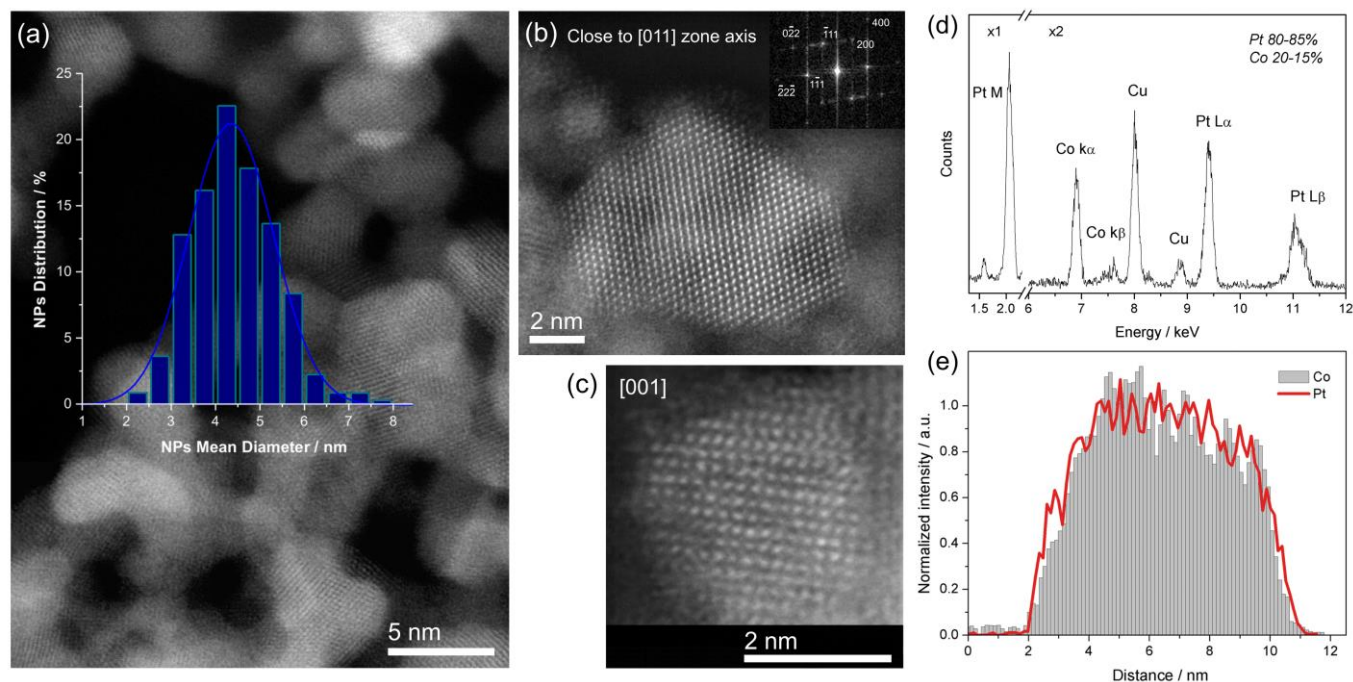

Figure 1. (a) HAADF-STEM image of a set of Co/Pt nanoparticles and the particle size distribution histogram. (b) Atomic-resolution STEM image of a particle closely aligned along the [011] zone axis and its FFT. (c) Single particle viewed along the [001] zone axis showing a certain loss of order in atomic positions at surface. (d) EDS spectrum of several particles evidencing a slight excess of Pt compared to the standard $CoPt_3$ structures. (e) Single particle STEM-EDS profile suggesting the presence of a surface Pt-rich $CoPt_3$ structures.

High-angle annular dark field (HAADF) images of the as-prepared particles were acquired using scanning transmission electron microscopy (STEM) in a Cs-corrected Titan 80/300 microscope operated at 300 kV. The particle distribution can be observed in Figure 1a. The mean particle size is about 4.4±1.9 nm, being calculated over a range of 350 particles. Figure 1b shows a high-resolution STEM image of an isolated particle close aligned to the [011] zone axis. The FFT (inset) analyses confirm the face-centered cubic (*fcc*) features of the particle (Figure 1b). The mean lattice parameter is estimated to be 0.3910 nm, which is in agreement with XRD analysis (see below). Another single particle is viewed in Figure 1c along the [001] zone axis. A certain loss of order in atomic positions at surface is observed.

The chemical composition of the particles was also probed with the assistance of Energy-Dispersive X-ray Spectroscopy (EDS) analyses over several particles (Figure 1d and 1e). The results show the presence of Co and Pt in a relative amount concentration of 15-20% and 80-85%, respectively (Figure 1d), indicating a slight excess of Pt when compared to standard $CoPt_3$ structures. Aiming to confirm these results, a single-particle EDS profile was also created (Figure 1e). A relative increase in the projected Pt concentration at the edge of the particle was observed, suggesting the presence of Pt-rich $CoPt_3$ surface structures.

The XRD analysis of these NPs (Figure 2) showed Bragg reflections corresponding to typical Pt face-centered cubic (*fcc*) features.[17]
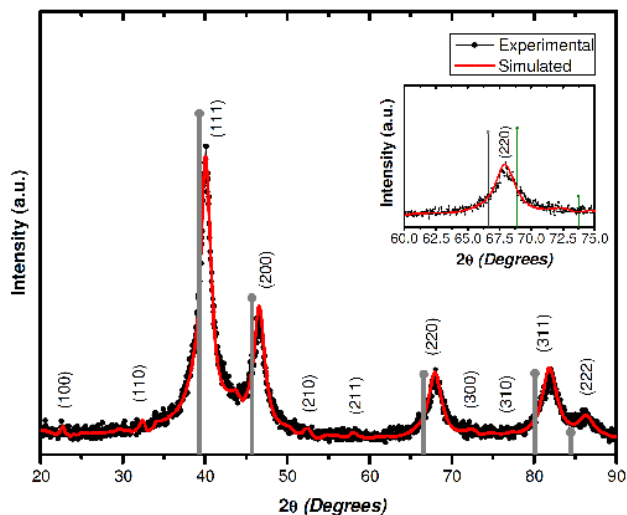

Figure 2. (a) XRD analysis of the bimetallic (Co/Pt) NPs prepared in $BMI.PF_6$ IL bulk *fcc* Pt (gray lines). Inset: 220 reflexes of bulk *fcc* Pt (gray line), $CoPt_3$@Pt like and $CoPt_3$ (green line) structures.

The five diffraction peaks are consistent with those of pure Pt metals with an *fcc* structure, corresponding to the (111), (200), (220), (311) and (222) planes. The peak positions

were shifted to higher angles, relative to Pt, indicating that Co was incorporated into the Pt *fcc* structure to form an alloy phase with a concomitant lattice contraction (0.38%). The XRD pattern showed (100) and (110) peaks characteristic of an ordered, inter-metallic $CoPt_3$@Pt-like structure.[17, 18] The average particle size of 4.7 nm, calculated using the full-width at half-maximum of the (220) diffraction and the Rietveld method, is similar than that measured using TEM micrographs (4.4±1.9 nm).

The relatively low temperature reduction (126 °C) of the NPs determined by temperature-programmed reduction (TPR) under hydrogen atmosphere (Figure 3a) suggests the surface Pt-rich NP surfaces.

Indeed, the reduction temperature of NPs containing sole Co prepared in the same IL[35] is much higher (>273°C). This is agreement with earlier related works in which Pt was found to significantly promote the reduction of base metal (Ni or Co). Influenced by hydrogen spillover, the reduction of Co ions shifted towards lower temperatures, as the reduced Pt atoms are able to dissociate hydrogen molecules into hydrogen atoms, leading to the accelerated reduction rate of Co ions.[36, 37]
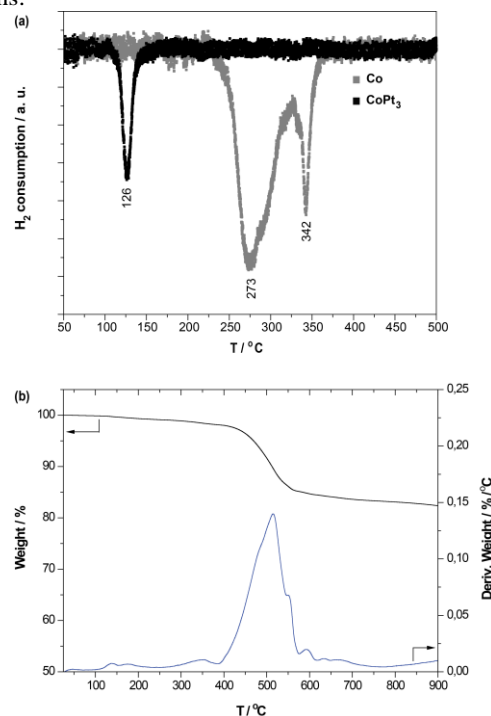

Figure 3. (a) Temperature programmed reduction (TPR) under hydrogen atmosphere profile of the Co and $CoPt_3$@Pt-like NPs. (b) Thermogravimetric analysis (TGA) of the $CoPt_3$@Pt-like NPs.

TGA curve of the isolated bimetallic NPs (Figure 3b) shows double stage weight loss owing to the evolution of adsorbed water in the temperature range up to 200 ºC and the second stage weight loss up to the temperature of around 380 ºC is

due to the decomposition of the IL.[38] The presence of water is due to the exposure of nanomaterial on air. The presence of organic material addressed to residual IL that could not be completely removed, as usually observed for MNPs prepared in these liquids.[39, 40] Indeed, the long scan XPS spectrum indicates the presence of fluorine and nitrogen, both coming from the ionic liquid used in the NPs synthesis process.

The $CoPt_3$@Pt like NPs exhibit super paramagnetic behavior (Figure 4) at room temperature and a very low coercivity, lower than that observed for $CoPt_3$ NPs[41] probably due to an increased Pt concentration.
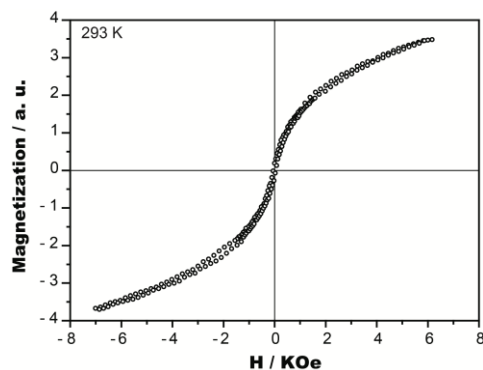

Figure 4. Dependence of the magnetization (M) on the magnetic field (*H*) for the isolated unsupported $CoPt_3$@Pt-like NPs of 4.4 ±1.9 nm.

The bimetallic NPs were submitted to a reduction treatment in a H_2 atmosphere followed by a sulfidation treatment using a H_2S atmosphere, both at 300°C.
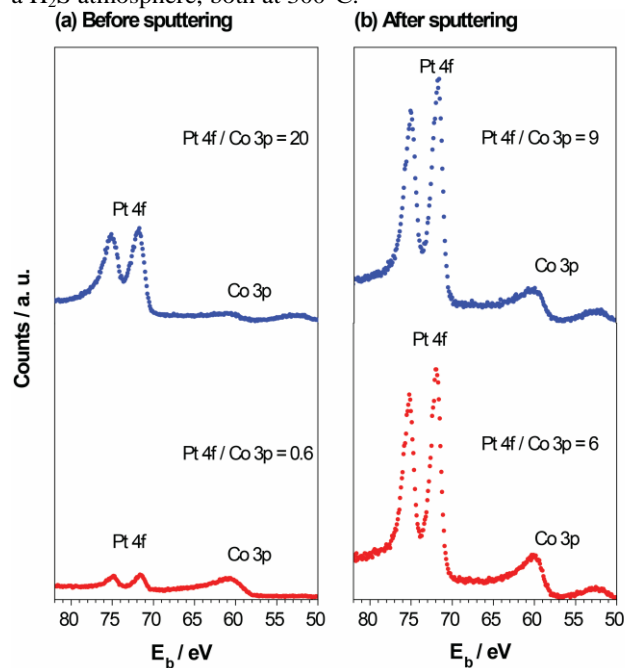

Figure 5. Pt 4f and Co 3p XPS regions for Co/Pt bimetallic NPs as prepared (blue points) and sulfided (red points) (a) before sputtering and (b) after sputtering cases.

XAS (X-Ray Absorption Spectroscopy) and XPS (X-Ray Photoelectron Spectroscopy) spectra were measured at the beginning (as prepared sample) and the end (reduction plus sulfidation at 300°C) of the processes. Pt 4f and Co 3p photoemission spectra for the as-prepared and sulfided samples were measured with photon energy of 1840 eV.

In order to probe the inner region of the nanoparticle, an ion sputtering was performed in the sample. This removed the outermost layers of the NPs, which enabled the XPS analysis of the inner region. Figure 5 displays the Pt 4f and Co 3p XPS spectra for the as-prepared (blue points) and sulfided (red points) samples before (a) and after (b) ion sputtering as well the XPS spectra for the sulfided sample before (c) and after (d) sputtering. The Pt 4f and Co 3p regions display photoemission peaks at similar kinetic energies and, consequently, comparable mean free paths of about 2 nm. In this way, the measurement allowed the relative intensity of the Pt and Co peaks to be monitored within the same probed range.
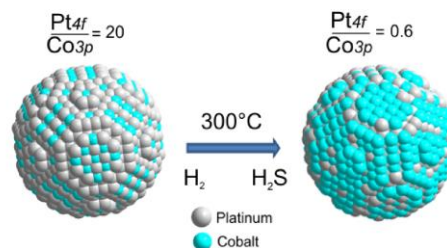
Scheme 1. Graphical representation of the atomic rearrangement induced by thermal treatment and sulfidation of the bimetallic $CoPt_3$@Pt-like NPs.

In order to probe the local order around the Pt and Co atoms, EXAFS measurements were performed in the as-prepared and sulfided samples in the transmission mode at the Pt L_3 (11564 eV) and Co K (7709 eV) edges. Figure 6 shows the EXAFS signals and the corresponding Fourier transform for the as-prepared (Figure 6a) and sulfided (Figure 6b) samples at the Pt L_3 edge and Co K edge. The gray lines represent the best fit of the data. The imaginary part (black points) is also displayed in order to demonstrate the good quality of the fitting achieved. Based on the XRD results, two phases in the fitting procedure (Pt and Co/Pt) and also a Pt-O and CoO contribution were considered.

Comparing the coordination number values obtained from the fitting procedure (see supporting information), there was a higher N_{Pt-Pt} value than for N_{Pt-Co} in the $CoPt_3$ phase (at the Pt L_3 edge) in the as-prepared and sulfided cases. This means that Pt atoms instead of Co atoms mostly surround the Pt atoms, which is consistent with the core-shell-like structure observed via XPS measurements. Analogously, the same behavior was observed for the Co K edge. In this case, the Co-Co scattering comes from the CoO phase (instead of the $CoPt_3$ phase) used in the fitting procedure. The migration of Co atoms to the skin layer during the thermal and gas treatment employed resulted in strong sulfidation of the Co

atoms, as observed by the high coordination number Co-S found (N_{Co-S} = 2.8 ± 0.1). On the other hand, Pt atoms are not surrounded by sulfur atoms (N_{Pt-S} = 0.2 ± 0.3) after the sulfidation treatment at 300°C.
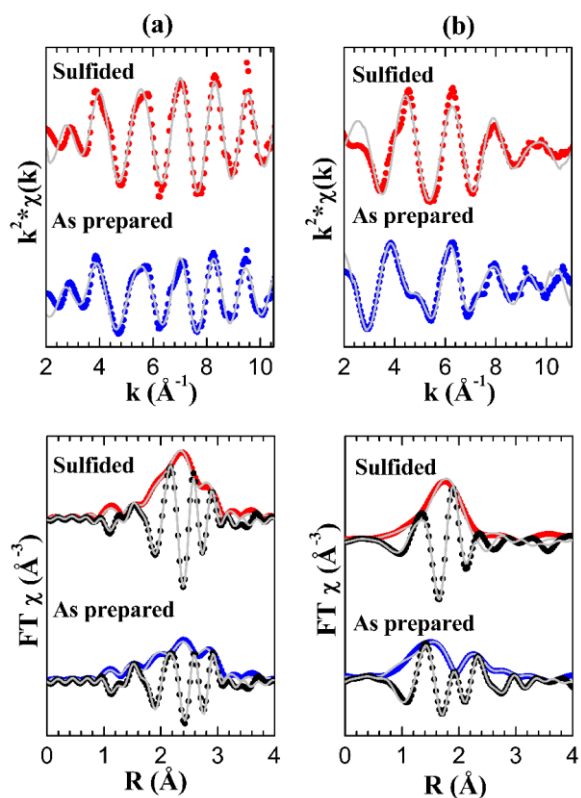

Figure 6. EXAFS signals and the corresponding Fourier transform at the (a) Pt L_3 edge and (b) Co K edge for the Co/Pt NPs as prepared and after the reduction plus sulfidation treatment at 300°C. The imaginary part of the Fourier transform is also displayed. The black points represent the experimental data, and the gray line indicates the fit.

The migration of Co atoms to the external layers during the thermal treatment was corroborated by the reactivity towards FTS. Thus, the isolated $CoPt_3@Pt$ alloy NPs were tested as catalysts in the FTS. The reaction of syngas (20 atm, H_2/CO = 2/1) using the unsupported bimetallic MNPs at 230°C for 16 h mainly produces hydrocarbons (53% of alkanes and 43% of alkenes and 4% of oxygenates) in the liquid phase. Methane was detected as the main product together with carbon dioxide and low-molecular-weight hydrocarbons in the gas phase (Figure 7). This is in contrast to that which was obtained with the monometallic unsupported Co MNPs for which methane was detected only in minor amounts on the gas-phase.[42] The hydrocarbons formed in the FTS with the bimetallic MNPs showed a hydrocarbon distribution of the naphta-fraction (< C10), which is quite different from the bimodal distribution (centered at C12 and C21) obtained with monometallic unsupported Co MNPs prepared in other ILs.[42] Moreover, monometallic unsupported cobalt

MNPs demonstrated selectivity for the formation of kerosene (C13 - C15) and diesel-like (C16-C20) products in the FTS.[35]

The deviation of ASF product distribution was detected, in particular, in the gas phase (Figure 8); i.e. C1 is formed in a greater quantity than that predicted by the ASF distribution, while a much lower amount of C2 is regularly reported.[43-47] The origin of this effect has been attributed to various factors such as the existence of multiple chain growth mechanisms; multiple different active sites on the catalyst; olefin re-adsorption and incorporation and, more recently, attributed concentration gradients caused by diffusion limitations in the catalyst, or on the reactor scale.[43-47] Nonetheless, the chain-growth probability was estimated using a modified Anderson–Schulz–Flory (ASF) equation, to give an ASF growth factor of 0.60 and 0.67 (Figure 7) suggesting the occurrence of two mechanisms: via carbene and CO insertion.[48-50]

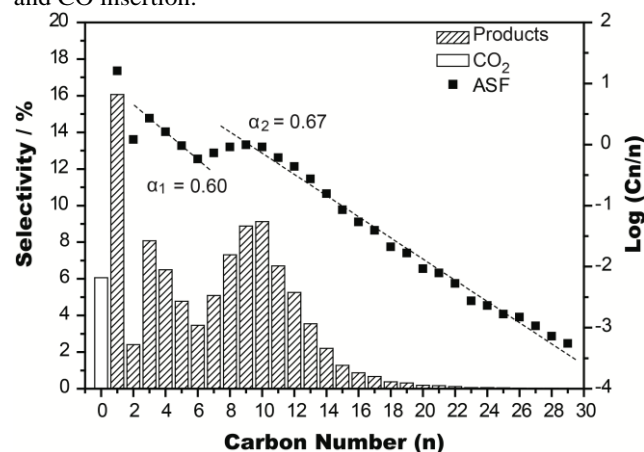**Figure 7**. ASF distribution from the FTS performed with Co/Pt NPs at 230 °C for 16 h and 20 atm (H_2/CO = 2/1).

Moreover, *in situ* IR spectrum of Co/Pt NPs after 16 h FTS reaction (Figure 8) display typical bands of CO adsorption at 1745 cm^{-1} (bridged mode), 1340 and 1260 cm^{-1} (assigned to the CO of carbonate), while terminal CO stretching lies under the free CO band at around 2110–2050 cm^{-1}.
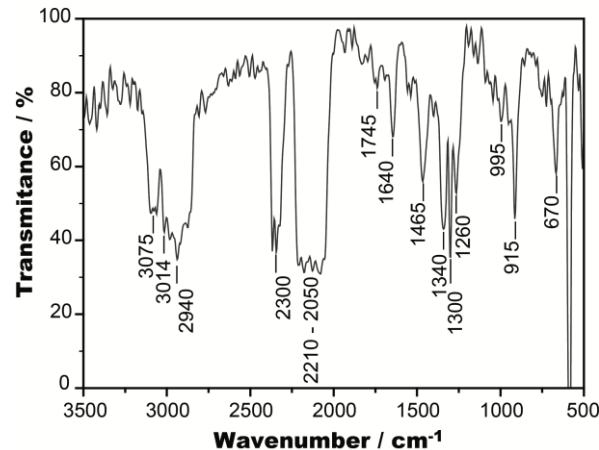
Figure 8. FTIR spectrum of the Co/Pt NPs, after 16 h FTS reaction.

More interesting are the bands at 1340, 1300 and 1260 cm^{-1}, which are typical of surface carbenes,[51] and those at 1640, 995 and 915 cm^{-1}, corresponding to $\nu_{C=C}$ vinylic, ν_{C-C} ethylidine and ρCH_2, respectively, which are typical of the adsorption of ethene to a metallic Pt surface.[52, 53] Therefore, the presence of these species also indicates that both mechanisms, i.e. via carbene and CO insertion, are operative.[49, 50] The observed catalytic activity can be explained by the formation of Co over-layer structures on CoPt$_3$@Pt-like NPs (induced by the thermal treatment) and from the change in the transition states of FT reactions imposed by the lattice mismatch between two metals.[15]

Conclusions

In summary, we have demonstrated that unsupported bimetallic CoPt$_3$@Pt-like NPs (4.7 nm in size) can be easily prepared by hydrogen reduction of Co(II) and decomposition of Pt(0) precursor in BMI.PF$_6$ IL. The TPR experiment shows the lower reduction temperature due to the rich-Pt surface. XAS measurements of the CoPt$_3$@Pt-like NPs were performed during reduction and sulfidation processes at 300°C. The vicinity of Pt atoms was modified by the elimination of lighter atoms after reduction and by the incorporation of S during sulfidation and migration of Co atoms toward the surface. The reduction and sulfidation processes induce an atomic rearrangement with the formation of a structure with a Co-enriched shell and a Pt-rich core. These CoPt$_3$@Pt-like nanomaterial displayed activity in the Fischer-Tropsch reaction under milder temperatures, and produced selectivity for the naptha products comparable to those achieved using Fe-HTFT technologies. The formation of Co over-layer structures on CoPt$_3$@Pt-like nanomaterial by the thermal treatment and the change of the transition states of FT reaction imposed by the lattice mismatch between two metals can explain the relative high activity and selectivity.

Experimental

General. All syntheses were performed using standard Schlenk techniques under argon atmosphere. Solvents were purified by standard procedures. Co(Cp)$_2$ was purchased from Sigma-Aldrich, and Pt$_2$(dba)$_3$ was prepared using known procedures.[54] Imidazolium ionic liquid was prepared following reported procedures.[55] H$_2$ (> 99.999%) and CO (> 99.999%) were purchased from White-Martins Ltd, Brazil. GC analyses were run with an Agilent GC System 6820. GC-MS analyses were run with a Shimadzu QP50 (EI = 70 eV). GC-TCD analyses were run with an Agilent MicroGC System 3000A. The magnetic properties of the isolated CoPt$_3$@Pt-like NPs were measured at room temperature with an AGM magnetometer. TGA analysis was run with a TA Instruments SDT Q600.

Synthesis of CoPt$_3$@Pt-like NPs. In a typical experiment, 28 mg (0.15 mmol) Co(Cp)$_2$ and 164 mg (0.15 mmol) Pt$_2$dba$_3$ were dissolved in BMI.PF$_6$ (1 mL). The mixture was placed in a stainless steel autoclave and then treated with 10 bar of H$_2$ at 150°C for 24 h. The material obtained was a black colloidal solution from which the NPs were isolated by centrifugation and extensive washing with dichloromethane (5 X 10 mL) to remove the impurities. The thus-obtained solid was dried under reduced pressure and used for the analysis and catalysis.

XRD analysis. The sample were characterized by X-ray diffraction using a Philips X'PERT diffractometer with Cu Kα(λ= 1.5418 Å) in a 2θrange from 20° to 90° with a step size of 0.05° and time of 1 s per step. Data processing was performed by the Rietveld method using FullProf software.[56] The instrumental resolution function (IRF) of the diffractometer was obtained from the LaB6 standard. The pseudo-Voigt profile function of Thompson, Cox and Hastings[57] was used with an asymmetry correction at low angles. The anisotropic size broadening effects, related to the coherence volume of diffraction, were simulated using a model of spherical harmonics.[56]

Temperature-programmed reduction (TPR). The TPR analyses were performed in quartz reactor (Micro Reactor CatLab® - Hidden Analytical), connected to a mass spectrometer (QIC 20® - Hidden Analytical), through a melt silica cannula. The experiments were performed with 10 mg of the material a 40 ml/min flux of 7% hydrogen in argon.

TEM Analyses. STEM were performed using an XFEG Cs-corrected FEI Titan 80/300 microscope at INMETRO operated at 300 kV. High Z-contrast images were acquired through STEM using a high-angle annular dark-field detector (HAADF) and semi-convergence angle of 27.4 mrad. The typical lateral resolution was greater than 0.01 nm. The images were processed with high frequency FFT-filters to reduce noise. EDS analyses were performed in STEM mode, allowing nanometer-scale spatial resolution. Spatial-correlated EDS profile experiments were carried out using K and L lines from Co and Pt, respectively. Particle size distributions were calculated from HAADF-STEM images over more than 350 particles.

XAS measurements.[58] For the XAS experiments, about 10 mg of the nanoparticle powder was compacted to produce 5-mm-diameter pellets. The pellet was introduced to the previously described reactor,[59] which allowed for controlled thermal treatment of the sample under controlled gas flow. Transmission mode measurements were performed at the LNLS (Brazilian Synchroton Light Laboratory) at the XAFS1 beamline.[58] The spectra were collected at the Pt L$_3$ and Co K edges using a channel-cut Si (111) crystal and three argon-filled ionization chambers. Standard Pt and Co foils were used to calibrate the monochromator. The spectra were acquired in the range of 11 440-12 200 eV (Pt L$_3$ edge) and 7610-8400 eV (Co K edge) with 2 eV steps and

2s/point. Two to four scans were acquired to improve the signal-to-noise ratio. All XAS spectra were measured at room temperature. The samples were submitted to (i) an increase in the temperature at a rate of 15°C/min under a He flux of 150 ml/min. (ii) After this, the reduction process was begun under a gas mixture of 5% He + 95% H_2 (total flux of 150 ml/min), for 30 min. (iii) After reduction, sulfidation was accomplished by flowing 95% He + 5% H_2S (total flux of 150 ml/min) for 30 min. XAS spectra were acquired at the end of the sulfidation process. The total gas pressure at the sample was kept at approximately 35 psi.

XPS measurements. After the sulfidation process and for the as-prepared case, the samples were introduced into the SXS beamline[60] endstation (also at LNLS), where XPS measurements were taken. The spectra were collected using an InSb (111) double crystal monochromator at a fixed photon energy of 1840 eV. The hemispherical electron analyzer (Physical Electronics model 10-360) was set at a pass energy of 23.5 eV, and the energy step was 0.1 eV, with an acquisition time of 500 ms/point. The base pressure used inside the chamber was about 1.0×10^{-9} mbar. The monochromator photon energy calibration was performed at the Si K edge (1839 eV). An additional calibration of the analyzer's energy was performed after every sample change using a standard Ag foil (Ag $3d_{5/2}$ peak at 368.3 eV). We also considered the C 1s peak value of 284.5 eV as a reference to verify possible charging effects. The samples were placed on carbon tape, and the XPS measurements were obtained at a 45° takeoff angle at room temperature. The samples were studied before and after ion sputtering using an Ar^+ ion beam at 3 keV for 10 min at a pressure of 4.0×10^{-6} mbar and impinging at a grazing incidence of 10° with respect to the sample surface. Data analysis: The EXAFS data were analyzed in accordance with the standard procedure of data reduction[61] using IFEFFIT.[62] FEFF was used to obtain the phase shift and amplitudes.[63] The EXAFS signal $\chi(k)$ was extracted then Fourier-transformed using a Kaiser-Bessel window with Δk range of 9.8 Å^{-1} (Pt L_3 edge) and 7.5 Å^{-1} (Co K edge). Single scattering events were considered in the fitting procedure. The S_0^2 was fixed at 0.86 (Pt) and 0.82 (Co) for all samples.

FTS reaction. The catalytic reaction using isolated NPs (10 mg) was performed in a DRIFT cell as reactor under 20 atm syngas (H_2/CO = 2/1) at 230°C for 16h. After reaction, the DRIFT cell was cooled at 25°C and connected to a Micro GC to analyze the gas phase. The liquid phase was dissolved in dichloromethane and analyzed by GC and GC-MS.

Acknowledgements

Notes and references

^{a} Institute of Chemistry – UFRGS – Av. Bento Gonçalves, 9500 – Porto Alegre – 91501-970 – RS – Brazil – Jairton.dupont@ufrgs.br
^{b} Institute of Physics – UFRGS - Av. Bento Gonçalves, 9500 – Porto Alegre – 91501-970 – RS – Brazil.

1. C. Burda, X. B. Chen, R. Narayanan and M. A. El-Sayed, *Chem. Rev.*, 2005, **105**, 1025-1102.
2. Z. H. Wei, J. M. Sun, Y. Li, A. K. Datye and Y. Wang, *Chem. Soc. Rev.*, 2012, **41**, 7994-8008.
3. V. R. Stamenkovic, B. Fowler, B. S. Mun, G. Wang, P. N. Ross, C. A. Lucas and N. M. Markovic, *Science*, 2007, **315**, 493-497.
4. V. R. Stamenkovic, B. S. Mun, M. Arenz, K. J. J. Mayrhofer, C. A. Lucas, G. Wang, P. N. Ross and N. M. Markovic, *Nature Mater.*, 2007, **6**, 241-247.
5. F. Tao, M. E. Grass, Y. W. Zhang, D. R. Butcher, F. Aksoy, S. Aloni, V. Altoe, S. Alayoglu, J. R. Renzas, C. K. Tsung, Z. W. Zhu, Z. Liu, M. Salmeron and G. A. Somorjai, *J. Am. Chem. Soc.*, 2010, **132**, 8697-8703.
6. F. Tao, S. R. Zhang, L. Nguyen and X. Q. Zhang, *Chem. Soc. Rev.*, 2012, **41**, 7980-7993.
7. K. L. More, K. S. Reeves and R. Borup, *Microsc. Microanal.*, 2009, **15**, 146-147.
8. J. Xu, X. Liu, Y. Chen, Y. Zhou, T. Lu and Y. Tang, *J. Mater. Chem.*, 2012, **22**, 23659-23667.
9. C.-T. Hsieh and J.-Y. Lin, *J. Power Sources*, 2009, **188**, 347-352.
10. G. Leteba and C. Lang, *Sensors*, 2013, **13**, 10358-10369.
11. G.-H. Wang, J. Hilgert, F. H. Richter, F. Wang, H.-J. Bongard, B. Spliethoff, C. Weidenthaler and F. Schüth, *Nature Mater.*, 2014, **13**, 293-300.
12. S. Koutsopoulos, K. Eriksen and R. Fehrmann, *J. Catal.*, 2006, **238**, 270-276.
13. A. Gual, C. Godard, S. Castillon, D. Curulla-Ferre and C. Claver, *Catal. Today*, 2012, **183**, 154-171.
14. F. Diehl and A. Y. Khodakov, *Oil Gas Sci. Technol. - Rev. IFP*, 2008, **64**, 11-24.
15. H. Wang, W. Zhou, J.-X. Liu, R. Si, G. Sun, M.-Q. Zhong, H.-Y. Su, H.-B. Zhao, J. A. Rodriguez, S. J. Pennycook, J.-C. Idrobo, W.-X. Li, Y. Kou and D. Ma, *J. Am. Chem. Soc.*, 2013, **135**, 4149-4158.
16. F.-J. Lai, W.-N. Su, L. S. Sarma, D.-G. Liu, C.-A. Hsieh, J.-F. Lee and B.-J. Hwang, *Chem. Eur. J.*, 2010, **16**, 4602-4611.
17. D. Wang, H. L. Xin, R. Hovden, H. Wang, Y. Yu, D. A. Muller, F. J. DiSalvo and H. D. Abruña, *Nature Mater.*, 2012, **12**, 81-87.
18. E. V. Shevchenko, D. V. Talapin, A. L. Rogach, A. Kornowski, M. Haase and H. Weller, *J. Am. Chem. Soc.*, 2002, **124**, 11480-11485.
19. L. Guczi, T. Hoffer, Z. Zsoldos, S. Zyade, G. Maire and F. Garin, *J. Phys. Chem.*, 1991, **95**, 802-808.
20. J.-I. Park and J. Cheon, *J. Am. Chem. Soc.*, 2001, **123**, 5743-5746.
21. Z. Zsoldos, T. Hoffer and L. Guczi, *J. Phys. Chem.*, 1991, **95**, 798-801.
22. W. Chu, L.-N. Wang, P. A. Chernavskii and A. Y. Khodakov, *Angew. Chem. Int. Ed.*, 2008, **47**, 5052-5055.
23. S. G. Kwon, G. Krylova, A. Sumer, M. M. Schwartz, E. E. Bunel, C. L. Marshall, S. Chattopadhyay, B. Lee, J. Jellinek and E. V. Shevchenko, *Nano Lett.*, 2012, **12**, 5382-5388.
24. J. D. Scholten, B. C. Leal and J. Dupont, *ACS Catal.*, 2012, **2**, 184-200.
25. H. Wender, P. Migowski, A. F. Feil, S. R. Teixeira and J. Dupont, *Coord. Chem. Rev.*, 2013, **257**, 2468-2483.
26. K. I. Okazaki, T. Kiyama, K. Hirahara, N. Tanaka, S. Kuwabata and T. Torimoto, *Chem. Commun.*, 2008, 691-693.
27. M. Prechtl and P. Campbell, *Nanotech. Rev.*, 2013, **2**, 577-595.
28. J. M. E. Pusch, D. Brondani, L. Luza, J. Dupont and I. C. Vieira, *Analyst*, 2013, **138**, 4898-4906.
29. T.-H. Tsai, S. Thiagarajan and S.-M. Chen, *J. Appl. Electrochem.*, 2009, **40**, 493-497.
30. I. S. Helgadottir, P. P. Arquillière, P. Bréa, C. C. Santini, P. H. Haumesser, K. Richter, A. V. Mudring and M. Aouine, *Microelectron. Eng.*, 2013, **107**, 229-232.
31. M. Hirano, K. Enokida, K. Okazaki, S. Kuwabata, H. Yoshida and T. Torimoto, *Phys. Chem. Chem. Phys.*, 2013, **15**, 7286-7294.

Nanoscale Accepted Manuscript

32. K. Schütte, A. Doddi, C. Kroll, H. Meyer, C. Wiktor, C. Gemel, G. van Tendeloo, R. A. Fischer and C. Janiak, *Nanoscale*, 2014, **6**, 5532.
33. K. Philippot and B. Chaudret, *Compt. Rend. Chim.*, 2003, **6**, 1019-1034.
34. J. Dupont, *Acc. Chem. Res.*, 2011, **44**, 1223-1231.
35. M. Scariot, D. O. Silva, J. D. Scholten, G. Machado, S. R. Teixeira, M. A. Novak, G. Ebeling and J. Dupont, *Angew. Chem. Int. Ed. Engl.*, 2008, **47**, 9075-9078.
36. G. Jacobs, T. K. Das, P. M. Patterson, J. L. Li, L. Sanchez and B. H. Davis, *Appl. Catal., A Gen.*, 2003, **247**, 335-343.
37. S. Vada, A. Hoff, E. Adnanes, D. Schanke and A. Holmen, *Top. Catal.*, 1995, **2**, 155-162.
38. H. L. Ngo, K. LeCompte, L. Hargens and A. B. McEwen, *Thermochim. Acta*, 2000, **357**, 97-102.
39. A. P. Umpierre, G. Machado, G. H. Fecher, J. Morais and J. Dupont, *Adv. Synth. Catal.*, 2005, **347**, 1404-1412.
40. G. Fonseca, J. Scholten and J. Dupont, *Synlett*, 2004, 1525-1528.
41. Y. Wang, X. Zhang, Y. Liu, Y. Jiang, Y. Zhang, J. Wang, Y. Liu, H. Liu, Y. Sun, G. S D Beach and J. Yang, *J. Phys. D: Appl. Phys.*, 2012, **45**, AN:485001.
42. D. Silva, J. Scholten, M. Gelesky, S. Teixeira, A. Dos Santos, E. Souza-Aguiar and J. Dupont, *ChemSusChem*, 2008, **1**, 291-294.
43. K. D. Kruit, D. Vervloet, F. Kapteijn and J. R. van Ommen, *Catal. Sci. Technol.*, 2013, **3**, 2210-2213.
44. C. M. Masuku, D. Hildebrandt and D. Glasser, *Chem. Eng. Sci.*, 2011, **66**, 6254-6263.
45. H. Schulz and M. Claeys, *Appl. Catal., A Gen.*, 1999, **186**, 91-107.
46. G. P. Van der Laan and A. Beenackers, *Cat. Rev. - Sci. Eng.*, 1999, **41**, 255-318.
47. C. G. Visconti, E. Tronconi, L. Lietti, P. Forzatti, S. Rossini and R. Zennaro, *Top. Catal.*, 2011, **54**, 786-800.
48. A. Y. C. Khodakov, W.; Fongarland, P., *Chem. Rev.*, 2007, **107**, 1692-1744.
49. J. Gaube and H. F. Klein, *J. Mol. Catal. A: Chem.*, 2008, **283**, 60-68.
50. J. Gaube and H. F. Klein, *Appl. Catal., A Gen.*, 2010, **374**, 120-125.
51. K. Nakamoto, *Infrared and Raman Spectra of Inorganic and Coordination Compounds*, John Wiley & Sons, New York, 1986.
52. F. Zaera, *Langmuir*, 1996, **12**, 88-94.
53. F. Zaera and N. Bernstein, *J. Am. Chem. Soc.*, 1994, **116**, 4881-4887.
54. T. O. Ely, C. Pan, C. Amiens, B. Chaudret, F. Dassenoy, P. Lecante, M. J. Casanove, A. Mosset, M. Respaud and J. M. Broto, *J. Phys. Chem. B*, 2000, **104**, 695-702.
55. P. A. Z. Suarez, J. E. L. Dullius, S. Einloft, R. F. DeSouza and J. Dupont, *Polyhedron*, 1996, **15**, 1217-1219.
56. J. Rodriguez-Carvajal, *Physica B*, 1993, **192**, 55-69.
57. P. Thompson, D. E. Cox and J. B. Hastings, *J. Appl. Crystallogr.*, 1987, **20**, 79-83.
58. H. C. N. Tolentino, A. Y. Ramos, M. C. M. Alves, R. A. Barrea, E. Tamura, J. C. Cezar and N. Watanabe, *J. Synchot. Rad.*, 2001, **8**, 1040-1046.
59. F. Bernardi, M. C. M. Alves, C. W. Scheeren, J. Dupont and J. Morais, *J. Electron. Spectrosc. Relat. Phenom.*, 2007, **156**, 186-190.
60. H. Tolentino, V. Compagnon-Cailhol, F. C. Vicentin and M. Abbate, *J. Synchot. Rad.*, 1998, **5**, 539-541.
61. D. C. Koningsberger and R. Prins, *X-ray Absorption: Principles, applications and techniques of EXAFS, SEXAFS and XANES in Chemical Analysis; Chemical Analysis*, John Wiley & Sons, New York, 1988.
62. M. Newville, *J. Synchot. Rad.*, 2001, **8**, 322-324.
63. S. I. Zabinsky, J. J. Rehr, A. Ankudinov, R. C. Albers and M. J. Eller, *Phys. Rev. B*, 1995, **52**, 2995-3009.

Graphical Abstract

Unsupported bimetallic Co/Pt nanoparticles (NP) of 4.4±1.9 nm prepared in ionic liquid undergoes the restructuration of the metal composition at the NP surface when they are submitted to hydrogen and posterior H_2S sulfidation.